



Cite this: *Phys. Chem. Chem. Phys.*,
2023, 25, 23717

Theoretical exploration on the performance of single and dual-atom Cu catalysts on the CO₂ electroreduction process: a DFT study†

Zhongze Bai,^a Xi Zhuo Jiang^{*b} and Kai H. Luo  ^{*a}

Carbon dioxide (CO₂) electroreduction by metal–nitrogen-doped carbon (MNC) catalysts is a promising and efficient method to mitigate global warming by converting CO₂ molecules to value-added chemicals. In this research, we systematically studied the behaviours of single and dual-atom Cu catalysts during the CO₂ electroreduction process using density functional theory (DFT) calculations. Two structures, *i.e.*, CuNC-4-pyridine and CuCuNC-4a, were found to be beneficial for C₂ chemical generation with relatively high stabilities. Subsequently, we explored the detailed pathways of key products (CO, HCOOH, CH₃OH, CH₄, C₂H₆O, C₂H₄ and C₂H₆) during CO₂ electroreduction on CuNC-4-pyridine and CuCuNC-4a. This research reveals the mechanisms of key product formation during CO₂ electroreduction on CuNC-4-pyridine and CuCuNC-4a, which would provide important insights to guide the design of MNC catalysts with low limiting potentials and high product selectivity.

Received 25th May 2023,
Accepted 8th August 2023

DOI: 10.1039/d3cp02403b

rsc.li/pccp

1. Introduction

Due to increasing fossil fuel consumption, CO₂ levels have increased in the atmosphere causing global warming.^{1,2} Electrochemical CO₂ reduction using clean renewable energy (sun, wind, *etc.*) is an effective approach to controlling CO₂ emissions. In this process, CO₂ from fossil fuels is converted to value-added chemicals and fuels achieving the carbon neural energy cycle,³ where O₂ is produced at the anode and CO₂ is reduced to organic matters at the cathode. At the same time, the hydrogen evolution reaction (HER) occurs at the cathode, which is a side reaction during the CO₂ reduction process and affects the reduction efficiency of CO₂. The main C₁ and C₂ products for CO₂ electroreduction are carbon monoxide (CO), methane (CH₄), formic acid (HCOOH), ethanol (C₂H₆O), ethylene (C₂H₄) and ethane (C₂H₆).⁴ Among them, C₂ products are more desirable due to their higher energy density and commercial values.^{5–7} Therefore, increasing the selectivity of C₂ product formation is of great interest.

Regarding catalysts, metal–nitrogen-doped carbon (MNC) materials are advanced and widely used catalysts for CO₂ electroreduction because of 100% atomic utilization, low coordination

environment of centre atoms, relatively uniform active sites, and adjustable and well-defined structures of active sites.⁸ Usually, the MNC structure consists of single metal atoms bonded with coordination atoms. Metal atoms are transition metals, and coordination atoms are non-metal elements. MNC materials with one and two atoms in the centre are called single-atom catalysts (SACs) and dual-atom catalysts (DACs), respectively. Among the many metallic elements, Cu-based catalysts are the only ones that can reduce CO₂ to C₂ products.⁸ Consequently, in this study, Cu based SACs and DACs were chosen as the target catalysts, and we explored their performance in product formation (especially C₂ products) during the CO₂ electroreduction process.

The investigation into CO₂ electroreduction facilitated by SACs and DACs has attracted a lot of interest in terms of both experiments and simulations over the last few years. For instance, Guan and co-workers studied the product distribution of Cu-SACs during the CO₂ electroreduction and the effects of the coordination environments of Cu atoms on CO₂ electroreduction performance through experiments and density functional theory (DFT) calculations.⁹ They found that two adjacent CuNC-2 sites and CuNC-4 coordination environments were favourable to generate C₂H₄ and CH₄, respectively.⁹ Karapinar and co-workers carried out a series of experiments and synthesised a CuNC material in a CuN₄ coordination environment to achieve aqueous CO₂ electroreduction with the highest faradaic yield among other Cu-based catalysts under optimized conditions.¹⁰ Ouyang and co-workers investigated the behaviours of DACs during the CO₂ electroreduction process and

^a Department of Mechanical Engineering, University College London, Torrington Place, London, WC1E 7JE, UK. E-mail: k.luo@ucl.ac.uk

^b School of Mechanical Engineering and Automation, Northeastern University, Shenyang, Liaoning, 110819, PR China. E-mail: jiangxz@mail.neu.edu.cn

† Electronic supplementary information (ESI) available. See DOI: <https://doi.org/10.1039/d3cp02403b>



observed that CO₂ can be efficiently reduced to CH₄ on CuCrNC-2 and CuMnNC-2 at low limiting potentials of −0.37 V and −0.32 V, respectively.¹¹ The energetically favourable formation of the C₃ product, acetone (CH₃COCH₃), during CO₂ electroreduction on CuNC-4-pyridine was found and proved by Zhao and co-workers through experiments and DFT calculations.¹² Wei and co-workers demonstrated that CuFeNC-3 is a high-performance CO₂ electroreduction catalyst for achieving multi-electro products like HCOOH, CH₃OH, and CH₄.¹³ Previous studies proved that Cu-based SACs and DACs show excellent performance in the CO₂ reduction process. However, their studies were mainly focused on C₁ products, with a lack of attention on higher value C₂ products. Besides, there has been a lack of systematic studies on the performance and stability of the structures of SACs and DACs, which are essential to the development of catalysts for efficient production of C₂ products during CO₂ electroreduction.

The aim of the current work is to systematically explore the behaviours of Cu-SACs and Cu-DACs during CO₂ electroreduction using density functional theory (DFT) calculations. First, we tested the stability of possible SAC and DAC structures. Second, the performance of C₂ products with stable structures was investigated and compared. Electron localization function (ELF) and charge density difference analyses were also carried out to reveal the stability mechanism and bonding nature of optimised structures with good C₂ chemical generation abilities. After that, the mechanisms of C₁ and C₂ products, such as CO, CH₄, HCOOH, C₂H₆O, C₂H₄ and C₂H₆, on selected catalysts (CuNC-4-pyridine and CuCuNC-4a) were illustrated. Finally, the electronic structures of selected catalysts were also analysed to further explain the effects of the coordination environments on the CO₂ reduction process.

2. Methods

2.1 DFT calculations

Spin-polarized DFT calculations were performed using the Vienna *Ab initio* Simulation Package (VASP)^{14,15} with generalized gradient approximation (GGA) and revised Perdew–Brueke–Ernzerhof (RPBE), which is optimised for adsorption energetic calculations.¹⁶ Plane wave energy cutoff and *k*-point grids were set to 500 eV and 3 × 3 × 1, respectively. van der Waals interaction was considered by adding the DFT-D3 method with Becke–Johnson damping.^{17,18} The convergence criteria for electronic energy and forces were 1.0 × 10^{−5} eV and 0.02 eV Å^{−1}, respectively. A vacuum slab of 20 Å was placed in the *Z*-axis direction to reduce periodic structure interaction. The computational hydrogen electrode (CHE) model^{19,20} was used to determine the change in Gibbs free energy (ΔG) of intermediates during the CO₂ electroreduction process. Electrolyte influence on the structure and energy of intermediates was considered using continuum solvation models by VASPsol code^{21–23} with relative permittivity $\epsilon_r = 78.4$, corresponding to that of water.²⁴ The cell size, lattice parameter and *k*-point mesh set in our work were selected based on previous work,²⁴ which were

demonstrated to provide reliable results in DFT calculations. The calculations were assisted by the VASPKIT²⁵ and QVASP²⁶ code. Crystal orbital Hamilton population (COHP) is calculated using Local Orbital Basis Suite Towards Electronic-Structure Reconstruction (LOBSTER).²⁷ For *ab initio* molecular dynamics (AIMD) calculations, all simulations were carried out below 300 K within 10 ps using the N ose–Hoover thermostat. The timestep was chosen as 1 fs. Other parameters were kept constant in DFT static computations.

2.2 Computational contents

The adsorption energy (E_{ads}) was calculated as shown in eqn (1).

$$E_{\text{ads}} = E_{\text{M/C}} - E_{\text{Catalyst}} - E_{\text{M}} \quad (1)$$

where, $E_{\text{M/C}}$, E_{C} , and E_{M} represent the total energy of the adsorbed molecule and catalyst, the energy of the catalyst, and the energy of adsorbates, respectively.

The Gibbs free energy (ΔG) change was calculated as follows:²⁸

$$\Delta G = \Delta E + \Delta E_{\text{ZPE}} - T\Delta S \quad (2)$$

ΔE is calculated directly from DFT calculations, and ΔE_{ZPE} and ΔS are the difference between the zero-point energy and entropy at temperature T . T is the room temperature (298.15 K) in the current study.

The limiting potential (U_{L}) is the minimal applied potential that ensures every step of an electrochemical process is exergonic, which is calculated by eqn (3):^{29–31}

$$U_{\text{L}} = -\Delta G_{\text{max}}/e \quad (3)$$

where ΔG_{max} denotes the free energy change of the potential limiting step (PLS) during the CO₂ reduction process at 0 V compared to the reversible hydrogen electrode (RHE).

Formation energy (E_{f}) is adopted to reveal the thermodynamic stabilities of all catalysts, which was calculated as follows:³²

$$\Delta E_{\text{f}} = E_{\text{Catalyst}} + a\mu_{\text{C}} - (E_{\text{gra}} + b\mu_{\text{N}} + 2\mu_{\text{Cu}}) \quad (4)$$

where E_{Catalyst} and E_{gra} are the total energies of optimised catalysts and pristine graphene with 72 atoms. μ_{C} and μ_{N} are the energies of a single carbon atom and a nitrogen atom, respectively, which were calculated from graphene and isolated N₂ molecules. μ_{Cu} is the energy of a single Cu metal atom in a vacuum. a is the number difference between the C atom in catalysts and pristine graphene. b is the number of N atoms in the catalysts.

Binding energy (E_{bin}) and cohesive energy (E_{coh}) were calculated to evaluate the binding behaviours between the N-doped graphene substrate and Cu atom, as shown in eqn (5) and (6),³³ respectively.

$$E_{\text{bin}} = (E_{\text{M/C}} - E_{\text{sub}} - n\mu_{\text{Cu}})/n \quad (5)$$

$$E_{\text{coh}} = E_{\text{bulk(Cu)}} - m\mu_{\text{Cu}} \quad (6)$$

where n and m are the number of Cu atoms in the catalysts and bulk Cu, respectively.



3. Results

3.1 Structures and stabilities of SACs and DACs

According to previous studies,^{34,35} there are two types of N atoms (pyridine nitrogen atom and pyrrole nitrogen atom) and the coordination numbers of central metal atoms can be either three or four. Thus, four types of SACs structures are considered, *i.e.*, CuNC-3-pyridine, CuNC-4-pyridine, CuNC-3-pyrrole and CuNC-4-pyrrole. For DACs, there are three coordination numbers for central metal atoms, which are two, three and four.^{13,32,36} They have three (CuCuNC-2a, CuCuNC-2b and CuCuNC-2c), one (CuCuNC-3) and three (CuCuNC-4a, CuCuNC-4b and CuCuNC-4c) possible configurations, respectively. The total of eleven optimized configurations for SACs and DACs are displayed in the ESI,[†] Fig. S1.

The stability of SACs and DACs mentioned above is assessed through the formation energies E_f and differences between the binding and cohesive energies E_{b-c} ($E_{b-c} = E_{bin} - E_{coh}$). The negative values of E_f and E_{b-c} indicate that catalysts are thermodynamically stable and metal atoms prefer to spread atomically on the graphene rather than aggregate into nanoparticles due to the coordination effect.³² The calculated results of E_f and E_{b-c} by eqn (4)–(6) are shown in Fig. 1. For SACs, coordination configurations of four-N and pyridine-N are more stable than those of three-N and pyrrole-N, respectively, which is in agreement with previous studies.^{8,35} All DACs structures are thermodynamically stable and enhance stability except for the structure with two-N coordination.

Among all tested structures, five have both negative E_f and E_{b-c} values, *i.e.*, CuNC-4-pyridine, CuCuNC-3, CuCuNC-4a, CuCuNC-4b and CuCuNC-4c. Additionally, 10 ps AIMD simulations at 300 K are carried out to examine the kinetic

stability of those configurations. As shown in the ESI,[†] Fig. S2, the structures of CuNC-4-pyridine, CuCuNC-3, CuCuNC-4a, CuCuNC-4b and CuCuNC-4c almost remain the same, though there are slight deformation, after AIMD simulations. This indicates these configurations have high kinetic stabilities.

3.2 C–C coupling energy barriers of catalysts

According to previous studies,^{24,37} C–C bond formation is the key step for C₂ chemical formation, which includes CO*–CO*, CO*–CHO* and CO*–COH* coupling pathways. C–C coupling is a non-electrochemical process and cannot be accelerated by the applied potential. The energy barriers of C–C bond formation play a vital role in C₂ product formation. The free energy barriers of C–C coupling as well as pathways CO* → CHO* and CO* → COH* for CuNC-4-pyridine, CuCuNC-3, CuCuNC-4a, CuCuNC-4b and CuCuNC-4c are presented in Fig. 2a and b, respectively. Due to the poor stability of the COH* intermediate on CuNC-4-pyridine, we did not consider CO–COH* coupling and the CO → COH* pathway for CuNC-4-pyridine configuration.

As described in Fig. 2a, pathways with negative free energy changes are observed in structures of CuNC-4-pyridine, CuCuNC-3, CuCuNC-4a and CuCuNC-4b during the C–C coupling process, which are CO–CHO*, CO–COH*, CO–CO* & CO–COH* and CO–COH*. For the CO* hydrogenation step, the energy barrier of COH* formation is significantly higher than that of CHO* (Fig. 2b), which means CHO* is more favourable than COH* during CO* hydrogenation. Therefore, in the current work, we chose configurations of CuNC-4-pyridine and CuCuNC-4a for further study, which are more desirable for C₂ chemical formation during the CO₂ electroreduction process.

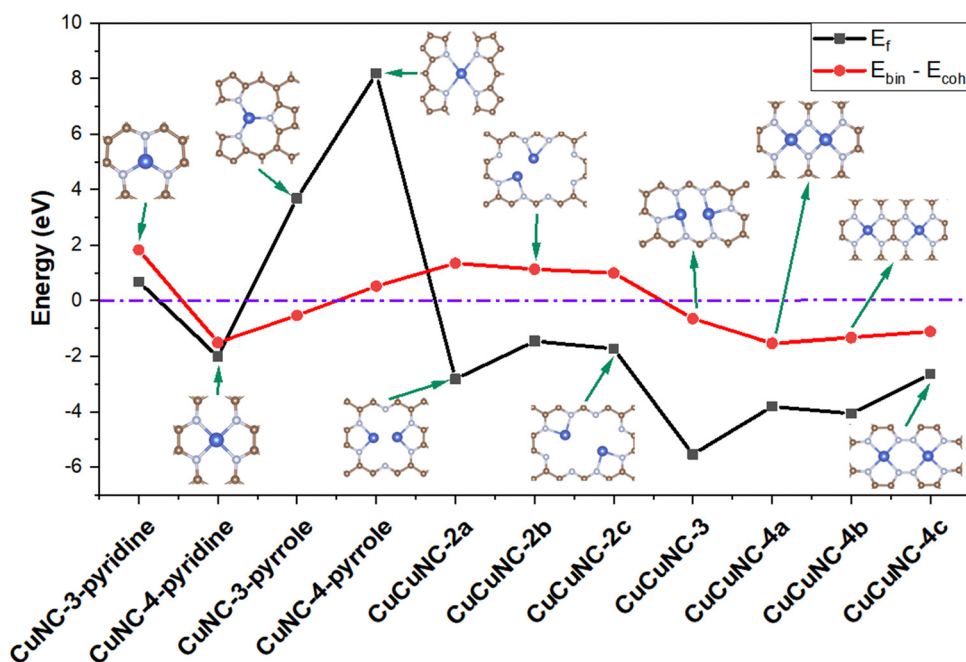


Fig. 1 Formation energies (E_f) and differences between the binding and cohesive energies of SACs and DACs ($E_{bin} - E_{coh}$).



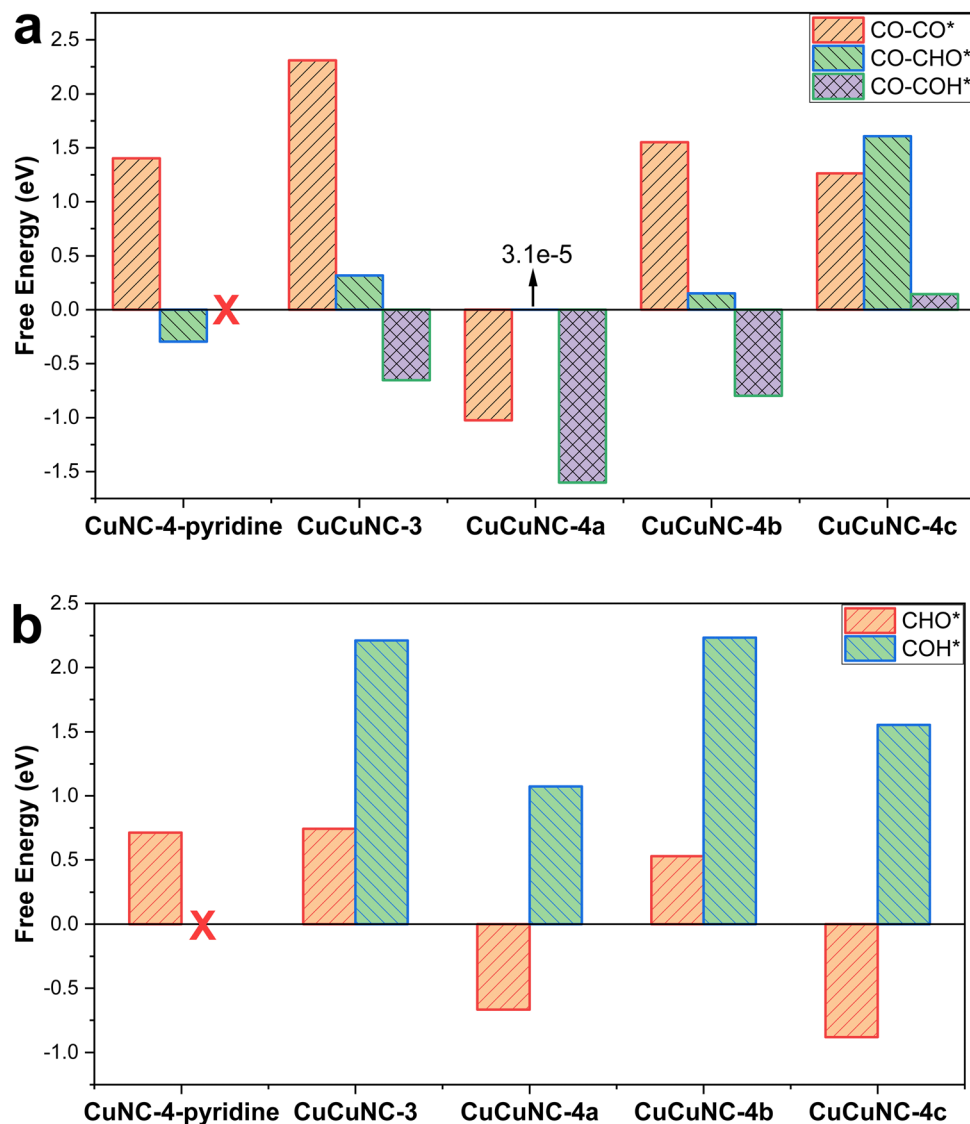


Fig. 2 Free energy changes for (a) CO^*-CO^* , CO^*-CHO^* and CO^*-COH^* coupling pathways, and (b) the hydrogenation step of CO^* to CHO^* and COH^* during the CO_2 electroreduction process (symbol * presents adsorbed state of intermediates). The X symbols in (a) and (b) mean the free energies of $\text{CO} \rightarrow \text{CO}-\text{COH}^*$ and $\text{CO} \rightarrow \text{COH}^*$ which are unavailable due to the instability of the COH^* intermediate on CuNC-4-pyridine.

3.3 The electronic properties of CuNC-4-pyridine and CuCuNC-4a

The electron localization function (ELF) is a tool in quantum chemistry used to analyze electron distribution and bonding properties. It identifies electron localization and delocalization, helps in understanding chemical reactivity, and characterizes bonding regions. On the other hand, the charge density difference study compares charge distributions between different systems, highlighting charge transfer, bonding changes, and intermolecular interactions, which aids in studying chemical reactions, material properties, and electronic stability. To explore the bonding nature of CuNC-4-pyridine and CuCuNC-4a, the electron local functions (ELFs) were calculated as shown in Fig. 3a and b. In general, a higher ELF value indicates greater local electronic distribution.³⁸ CuNC-4-pyridine and CuCuNC-

4a have ELF values between 0.7 and 1.0, indicating that Cu is fixed in the surrounding N atomic centres by chemisorption. These findings are consistent with the stability analysis through E_f and E_{b-c} in Section 3.1. Charge density differences in Fig. 3c and d, as well as Bader charge analysis in the ESI,[†] Table S1, reveal that in CuNC-4-pyridine and CuCuNC-4a, electrons will transfer from Cu to N to generate stable covalent bonds. These findings also explain the strong coordination interaction at the electronic level between Cu and the stable structures of CuNC-4-pyridine and CuCuNC-4a configurations. This information is helpful for understanding electronic structures, bonding, and reactivity, providing valuable insights for materials design, reaction mechanisms, determination of the stability of catalysts and selection of the adsorption sites for intermediates.



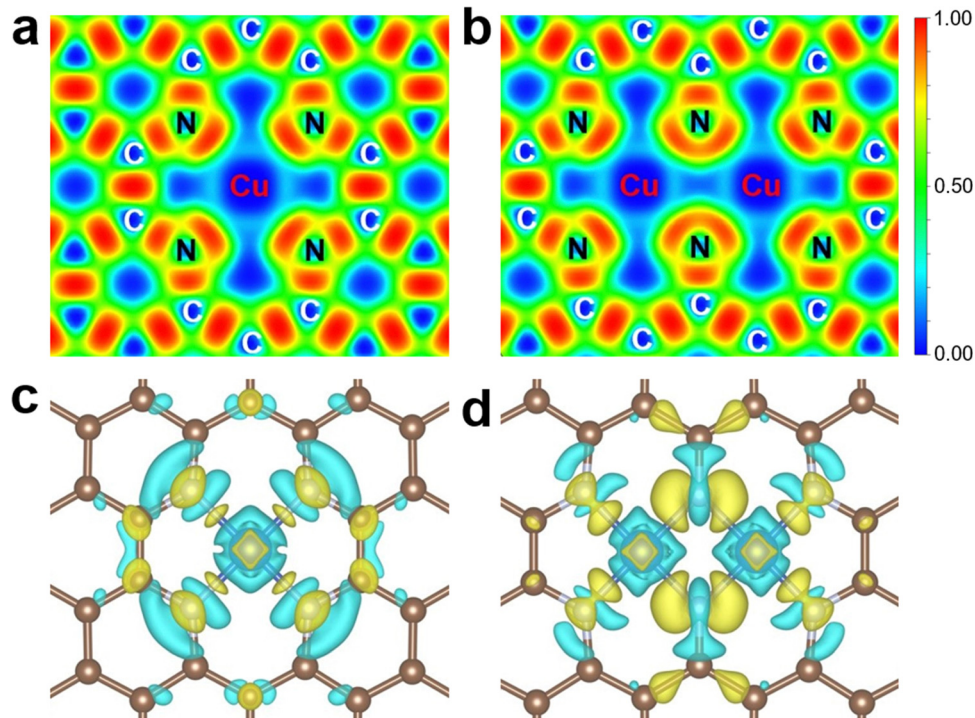


Fig. 3 Electron localization function (ELF) of (a) CuNC-4-pyridine and (b) CuCu-NC-4a. Charge density difference of (c) CuNC-4-pyridine and (d) CuCu-NC-4a. The isosurface value is $0.004 \text{ e bohr}^{-3}$. Yellow and blue regions represent increasing and decreasing electron densities, respectively.

3.4 CO₂ electroreduction to C₁ and C₂ products through CuNC-4-pyridine

Due to the wide range of CO₂ electrolysis products, detailed transfer pathways for CO₂ electroreduction are of great importance to efficiently control the electrocatalytic process of CO₂ into specific products. The possible pathways used in the present work refer to previous studies,^{39–41} as shown in the ESI,[†] Fig. S4. Due to the poor stability of COH* intermediates on CuNC-4-pyridine, pathways related to COH* are not considered. For C₂ product generation, only the route linked to CO-CHO is considered. The free energies of these possible steps are listed in the ESI,[†] Table S2.

After calculating all possible pathways, we obtained the most favourable reaction pathways with the lowest limiting potential of CO₂ electroreduction on CuNC-4-pyridine, as illustrated in Fig. 4. The optimized intermediates for CO₂ electroreduction on the CuNC-4-pyridine site are presented in the ESI,[†] Fig. S5. Overall, the high adsorption energy of CO₂ molecules ($E_{\text{ads}}(\text{CO}_2)$, $\text{CO}_2 \rightarrow \text{CO}_2^*$) inhibits CO₂ electroreduction to C₁ and C₂ chemicals. As shown in Fig. 4a, the pathways for CO, HCOOH, CH₃OH, and CH₄ are *via* $\text{CO}_2 \rightarrow \text{CO}_2^* \rightarrow \text{COOH}^* \rightarrow \text{CO}^* \rightarrow \text{CO}$, $\text{CO}_2 \rightarrow \text{CO}_2^* \rightarrow \text{OCHO}^* \rightarrow \text{HCOOH}^* \rightarrow \text{HCOOH}$, $\text{CO}_2 \rightarrow \text{CO}_2^* \rightarrow \text{OCHO}^* \rightarrow \text{HCOOH}^* \rightarrow \text{CHO}^* \rightarrow \text{CH}_2\text{O}^* \rightarrow \text{CH}_3\text{O}^* \rightarrow \text{CH}_3\text{OH}^* \rightarrow \text{CH}_3\text{OH}$, and $\text{CO}_2 \rightarrow \text{CO}_2^* \rightarrow \text{OCHO}^* \rightarrow \text{HCOOH}^* \rightarrow \text{CHO}^* \rightarrow \text{CH}_2\text{O}^* \rightarrow \text{CH}_3\text{O}^* \rightarrow \text{CH}_3\text{OH}^* \rightarrow \text{OH}^* + \text{CH}_4 \rightarrow \text{H}_2\text{O}^* \rightarrow \text{H}_2\text{O}$, respectively. The step $\text{CO}_2^* \rightarrow \text{COOH}^*$ limits the CO formation with U_L of -1.07 eV . The critical step for HCOOH is $\text{CO}_2^* \rightarrow \text{OCHO}^*$ with U_L of -0.44 eV . The conversion from HCOOH* to CHO* with U_L of -0.68 eV

limits the formation of CH₃OH and CH₄. The conversions from CH₃OH* to CH₃OH and to CH₄ + OH* are downhill and uphill processes, respectively. CH₃OH is a more favourable product than CH₄. Thus, the difficulty of C₁ product generation on CuNC-4-pyridine is HCOOH, CH₃OH, CH₄ and CO in increasing order.

As shown in Fig. 4b, step $\text{CO}_2 \rightarrow \text{COOH}^*$ is the limiting step for all C₂ products (CH₃CH₂OH, C₂H₄ and C₂H₆). The route $\text{CO}_2 \rightarrow \text{CO}_2^* \rightarrow \text{COOH}^* \rightarrow \text{CO}^* \rightarrow \text{CHO}^* \rightarrow \text{CHO-CO}^* \rightarrow \text{CHO-CHO}^* \rightarrow \text{CHO-CHOH}^* \rightarrow \text{CH-CHO}^* \rightarrow \text{CH-CHOH}^*$ is the common route for all C₂ product formation. The unique pathways for CH₃CH₂OH, C₂H₄ and C₂H₆ generation are $\text{CH-CHOH}^* \rightarrow \text{CH}_2\text{-CHOH}^* \rightarrow \text{CH}_2\text{-CH}_2\text{OH}^* \rightarrow \text{CH}_3\text{-CH}_2\text{OH}^* \rightarrow \text{CH}_3\text{-CH}_2\text{OH}$, $\text{CH-CHOH}^* \rightarrow \text{CH-CH}^* \rightarrow \text{CH}_2\text{-CH}^* \rightarrow \text{CH}_2\text{-CH}_2^* \rightarrow \text{C}_2\text{H}_4$, and $\text{CH-CHOH}^* \rightarrow \text{CH-CH}^* \rightarrow \text{CH}_2\text{-CH}^* \rightarrow \text{CH}_3\text{-CH}^* \rightarrow \text{CH}_3\text{-CH}_2^* \rightarrow \text{CH}_3\text{-CH}_3^* \rightarrow \text{C}_2\text{H}_6$, respectively. The ΔG for $\text{CH}_3\text{-CH}_2\text{OH}^* \rightarrow \text{CH}_3\text{-CH}_2\text{OH}$ and $\text{CH}_3\text{-CH}_3^* \rightarrow \text{C}_2\text{H}_6$ are positive, indicating that CH₃CH₂OH and C₂H₆ are not easy to desorb from the CuNC-4-pyridine catalyst, and the desorption process is also a non-electrochemical process that will hinder the formation of CH₃CH₂OH and C₂H₆. Thus, the difficulty of C₂ chemicals formation is C₂H₄, C₂H₆O and C₂H₆ in a descending order. Moreover, CO* is an important precursor for the formation of C₂ products. Compared to the formation of CO ($\text{CO}^* \rightarrow \text{CO}$), a free energy drop process, CO* has to undergo a free energy rise to produce CHO* for C₂ chemical formation at the initial stage. Thus, the formation of C₂ is more difficult than that of CO (and other C₁ products).

H₂ formation on the cathode is an important competitive reaction during the CO₂ electroreduction process. U_L of the



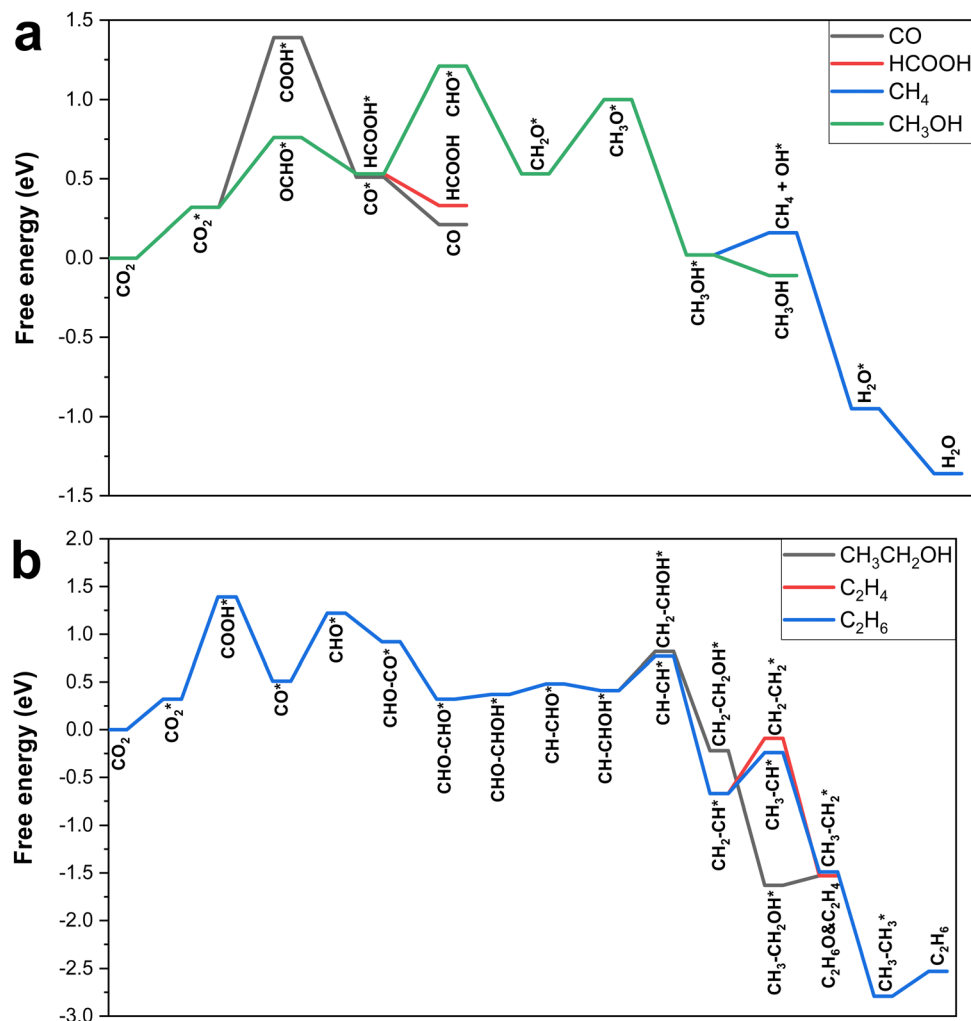


Fig. 4 Most favourable reaction pathways of CO_2 electroreduction to C_1 and C_2 chemicals on CuNC-4-pyridine at 0 applied voltage (symbol * presents the adsorbed state of intermediates).

HER on CuNC-4-pyridine is -0.80 eV, which is higher than those of HCOOH, CH_3OH and CH_4 . The high energy suggests that CuNC-4-pyridine can inhibit the H_2 formation for the generation of HCOOH, CH_3OH and CH_4 , which contributes to the CO_2 reduction.

3.5 CO_2 electroreduction to C_1 and C_2 products through CuCu-NC-4a

The possible pathways of C_1 and C_2 products during CO_2 electroreduction can be inferred from previous studies^{39–41} (Fig. S4, ESI†). Among the possible pathways of C_2 chemicals, the most likely C–C coupling route of CO–CO is considered. The free energies of possible elementary steps are listed in the ESI,† Table S2. The most favourable pathways of CO_2 electroreduction to C_1 and C_2 chemicals on CuCuNC-4a are shown in Fig. 5a and b, respectively. The optimized intermediates on the CuCuNC-4a site are presented in the ESI,† Fig. S6.

For C_1 product formation, the channels for CO, HCOOH, CH_3OH and CH_4 formation are $\text{CO}_2 \rightarrow \text{CO}_2^* \rightarrow \text{COOH}^* \rightarrow \text{HCOOH}^* \rightarrow \text{HCOOH}$, $\text{CO}_2 \rightarrow \text{CO}_2^* \rightarrow \text{COOH}^* \rightarrow \text{CO}^* \rightarrow \text{CO}$,

$\text{CO}_2 \rightarrow \text{CO}_2^* \rightarrow \text{COOH}^* \rightarrow \text{HCOOH}^* \rightarrow \text{HCOOH}$, $\text{CO}_2 \rightarrow \text{CO}_2^* \rightarrow \text{COOH}^* \rightarrow \text{HCOOH}^* \rightarrow \text{CHO}^* \rightarrow \text{CHOH}^* \rightarrow \text{CH}_2\text{OH}^* \rightarrow \text{CH}_3\text{OH}^* \rightarrow \text{CH}_3\text{OH}$ and $\text{CO}_2 \rightarrow \text{CO}_2^* \rightarrow \text{COOH}^* \rightarrow \text{HCOOH}^* \rightarrow \text{CHO}^* \rightarrow \text{CHOH}^* \rightarrow \text{CH}_2\text{OH}^* \rightarrow \text{CH}_3\text{OH}^* \rightarrow \text{CH}_4 + \text{OH}^* \rightarrow \text{H}_2\text{O}^* \rightarrow \text{H}_2\text{O}$, respectively. $\text{COOH}^* \rightarrow \text{CO}^*$ is the limiting step for CO formation with U_L of -0.22 eV. The critical step of HCOOH formation is the conversion from $\text{COOH}^* \rightarrow \text{HCOOH}^*$ ($U_L = -0.10$ eV). U_L for CH_3OH and CH_4 remains the same, which is -0.51 eV *via* pathway $\text{CHO}^* \rightarrow \text{CHOH}^*$. Considering the energy barrier of $\text{CH}_3\text{OH}^* \rightarrow \text{CH}_4 + \text{OH}^*$ is significantly higher than that of $\text{CH}_3\text{OH}^* \rightarrow \text{CH}_3\text{OH}$, the CH_3OH formation is more likely to happen than CH_4 . Thus, the difficulty in C_1 product generation is HCOOH, CO, CH_3OH and CH_4 in descending order.

According to Fig. 5b, conversion from CO_2 to $\text{CH}_2\text{-CHOH}^*$ is the common route for C_2 -product ($\text{C}_2\text{H}_6\text{O}$, C_2H_4 and C_2H_6) generation, which is $\text{CO}_2 \rightarrow \text{CO}_2^* \rightarrow \text{COOH}^* \rightarrow \text{CO}^* \rightarrow \text{CO-CO}^* \rightarrow \text{CO-CHO}^* \rightarrow \text{CHO-COH}^* \rightarrow \text{CHOH-COH}^* \rightarrow \text{CH-COH}^* \rightarrow \text{CH}_2\text{-COH}^* \rightarrow \text{CH}_2\text{-CHOH}^*$. The pathways for $\text{CH}_3\text{CH}_2\text{OH}$, C_2H_4 and C_2H_6 formation are $\text{CH}_2\text{-CHOH}^* \rightarrow$



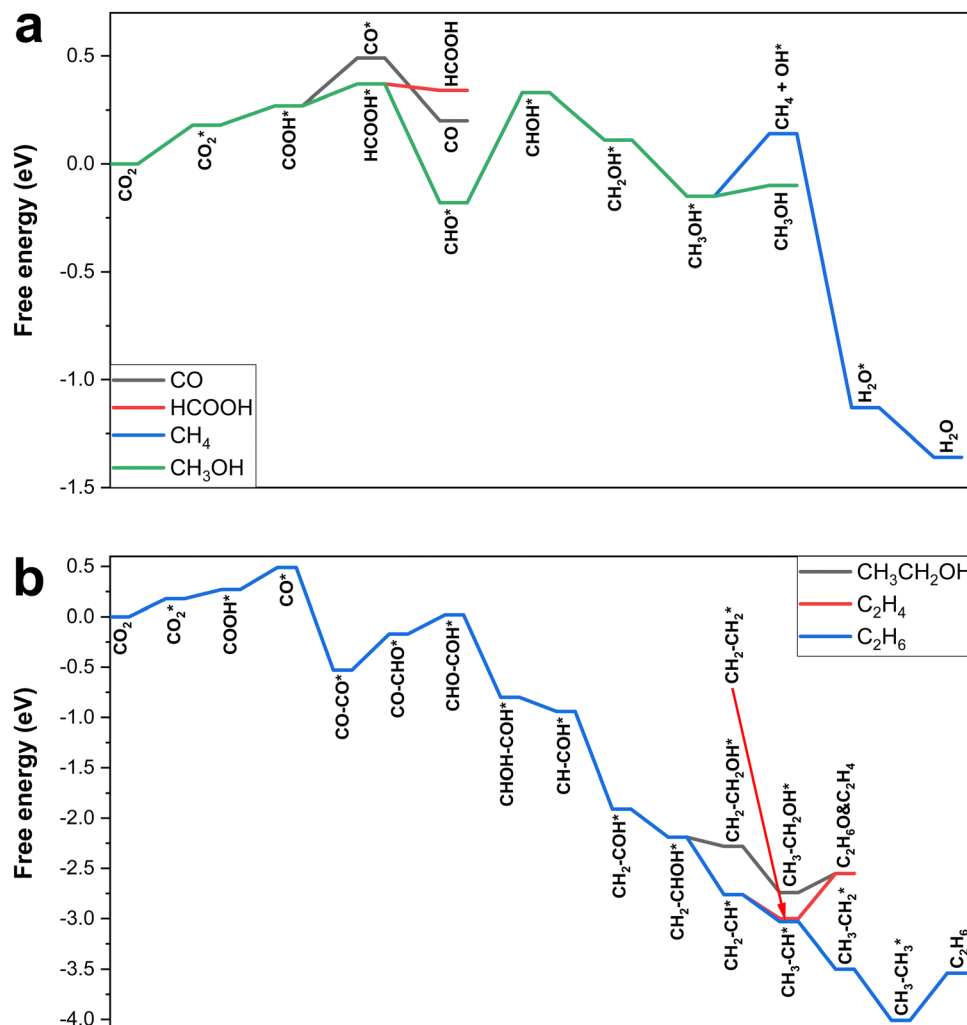


Fig. 5 Most favourable reaction pathways of CO_2 electroreduction to C_1 and C_2 chemicals on CuCuNC-4a at 0 applied voltage (symbol * presents adsorbed state of intermediates).

$\text{CH}_2\text{-CH}_2\text{OH}^* \rightarrow \text{CH}_3\text{-CH}_2\text{OH}^* \rightarrow \text{C}_2\text{H}_6\text{O}$, $\text{CH}_2\text{-CHOH}^* \rightarrow \text{CH}_2\text{-CH}^* \rightarrow \text{CH}_2\text{-CH}_2^* \rightarrow \text{C}_2\text{H}_4$ and $\text{CH}_2\text{-CHOH}^* \rightarrow \text{CH}_2\text{-CH}^* \rightarrow \text{CH}_3\text{-CH}^* \rightarrow \text{CH}_3\text{-CH}_2^* \rightarrow \text{CH}_3\text{-CH}_3^* \rightarrow \text{C}_2\text{H}_6$, respectively. The limiting step for C_2 product formation is $\text{CO-CO}^* \rightarrow \text{CO-CHO}^*$ with an U_L of -0.36 eV. The CO-CO^* coupling energy barrier is lower than that of $\text{CO}^* \rightarrow \text{CO}$, indicating that C_2 chemical formation is more likely than that of CO molecules. However, E_{ads} values for $\text{C}_2\text{H}_6\text{O}$, C_2H_4 and C_2H_6 are -0.19 eV, -0.45 eV and -0.47 eV, respectively. This limits the formation of C_2 products during the CO_2 electroreduction process. And the difficulties in C_2 chemical formation is $\text{C}_2\text{H}_6\text{O}$, C_2H_4 and C_2H_6 in descending order. Finally, U_L for H_2 formation is -0.10 eV, which is the same as that for HCOOH formation and lower than that for other products. To increase the conversion rate of C_1 and C_2 chemicals, the production of H_2 during the CO_2 electrolysis process should be prohibited.

3.6 Origin of catalytic activity of CuNC-4-pyridine and CuCuNC-4a

Based on the above analysis, in general, the intermediate has lower adsorption energy on CuCuNC-4a compared to

CuNC-4-pyridine. To further explain the difference in the CO_2 reduction characteristics of CuNC-4-pyridine and CuCuNC-4a, we selected the intermediate COOH as a representative for electronic analysis. Fig. 6 shows the charge density difference of adsorbed COOH on CuNC-4-pyridine and CuCuNC-4a, respectively. The Bader charges are listed in the ESI,[†] Table S1, and position numbers of C, N, Cu, O and H atoms on CuNC-4-pyridine and CuCuNC-4a and COOH are presented in the ESI,[†] Fig. S7. According to Fig. 6, COOH adsorbs to CuNC-4-pyridine by generating the Cu-C bond with the Cu atom and electrons are transferred from the Cu atom to C atom. However, COOH forms a C-N bond with the N5 atom on CuCuNC-4a with electrons transferring from the C atom to N atom. And the bond length of Cu-C (1.93 Å) is longer than that of N-C (1.39 Å), indicating CuCuNC-4a adsorbs COOH more strongly than CuNC-4-pyridine.

Fig. 7a and b display partial density of states (PDOS) of Cu and N atoms on CuNC-4-pyridine and CuCuNC-4a without COOH adsorbed. Bond centers of Cu, N and C atoms are shown in the ESI,[†] Table S3. PDOS values of N1 to N4 are the same and the 2p bond center is -3.8 eV. The Cu-3d bond center is



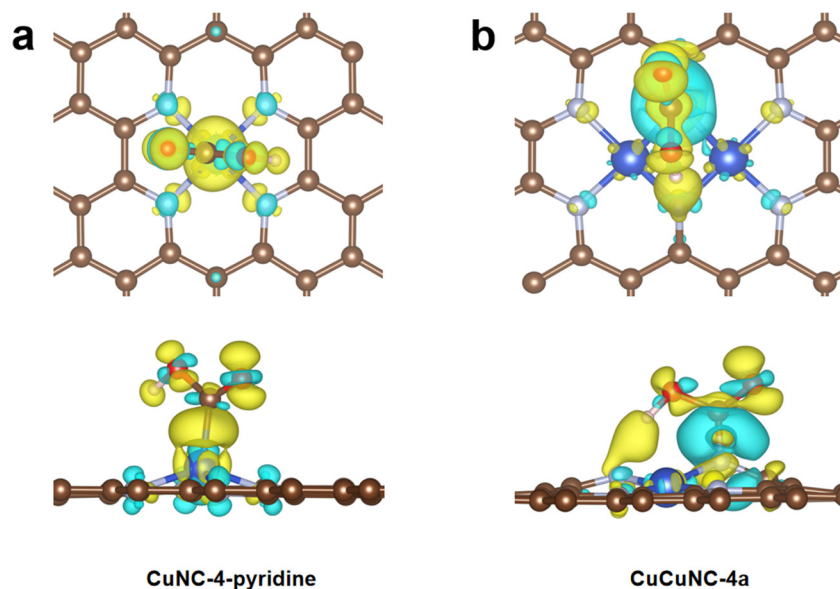


Fig. 6 Charge density difference of adsorbed COOH on (a) CuNC-4-pyridine and (b) CuCu-NC-4a. The isosurface value is $0.004 \text{ e bohr}^{-3}$. Yellow and blue regions represent increasing and decreasing electron densities, respectively.

–3.2 eV, which is closer to the Fermi energy level (0 eV) than that of N. That means Cu has a stronger interaction with intermediates, which is consistent with the result in Fig. 6a that COOH adsorbed on the Cu atom of CuNC-4-pyridine. For CuCuNC-4a, the PDOS values of N1&N3&N4&N6 remain the same, which are different from N2&N5 with 2p band centers of –3.9 eV and –2.8 eV, respectively. Cu1 and Cu2 share the same PDOS value with a 3d band center of –3.1 eV. Among them, the bond center of N2&N5 is the closest to the Fermi energy level, agreeing well with the adsorption site for COOH on CuCuNC-4a. Fig. 7c and d partial density of states (PDOS) of adsorbed COOH on CuNC-4-pyridine with Cu and C atoms and CuCu-NC-4a with N and C atoms. The C-2p center in CuCuNC-4a (–2.2 eV) is closer to the Fermi energy level than that of CuNC-4-pyridine (–2.5 eV). And the hybridization between C-2p and N-2p is more apparent than that between Cu-3d. This indicates the N–C interaction is stronger than that of Cu–C.

To better illustrate the interaction of COOH with catalysts, we calculated the COHP between the Cu atom on CuNC-4-pyridine as well as the N atom on CuCuNC-4a and C atoms (COOH) on catalysts, respectively. The curve on the right side is the bonding side and the antibonding side is on the left. The orbital interactions between Cu and C are weaker than those between N and C as more antibonding states occur below the Fermi level in CuNC-4-pyridine. Then, the integrated-COHP is calculated as shown in the ESI,† Table S4. CuCuNC-4a has more negative ICOHP and correspondingly lower COOH adsorption energy, again demonstrating the stronger adsorption of CuCuNC-4a to COOH. In summary, CuCuNC-4a presents strong adsorption to intermediates because of its shorter bond length, higher bond center and stronger orbital interactions between N and C atoms.

4. Discussion

In the present study, we explored the behaviours for the product formation of CuNC-4-pyridine and CuCuNC-4a, which have the abilities to benefit C_2 product formation among Cu-SACs and Cu-DACs. The novelty of the present study manifests in two aspects: first, to our best knowledge, the performance of the CuCu-NC-4a catalyst is investigated, for the first time; second, the formation of C_2 products on CuNC-4-pyridine and CuCu-NC-4a is systematically investigated in the present study, while previous studies only focused on the formation of C_1 products on CuNC-4-pyridine. Our simulations agree well with a previous study on free energy changes and intermediate adsorption sites,¹² although there are some differences in the specific values of free energy variations. The differences mainly come from the discrepancies in the simulated parameters. In our simulations, we adopted higher values of the plane wave cutoff energy and k -point sampling, took van der Waals interaction and solvation effects into consideration, and used a revised Perdew–Bruke–Ernzerhof function that is specific for adsorption energy calculations.

To select a better catalyst for C_2 products during the CO_2 electroreduction process, we compare the free energy of key products generated on CuNC-4-pyridine and CuCuNC-4a. Table 1 shows U_L and E_{ads} of the main products generated on CuNC-1-pyridine and CuCuNC-4a catalysts. Overall, the limiting potential and E_{ads} values of CuCuNC-4a are lower than those of CuNC-4-pyridine, which means that CuCuNC-4a is a preferable catalyst featuring higher energy utilisation by applying a lower voltage. However, a lower U_L of H_2 on CuCuNC-4a means that the competitive reaction, H_2 production, is intense and needs to be inhibited to enhance the efficiency of CO_2 reduction. CuCuNC-4a also decreases E_{ads}



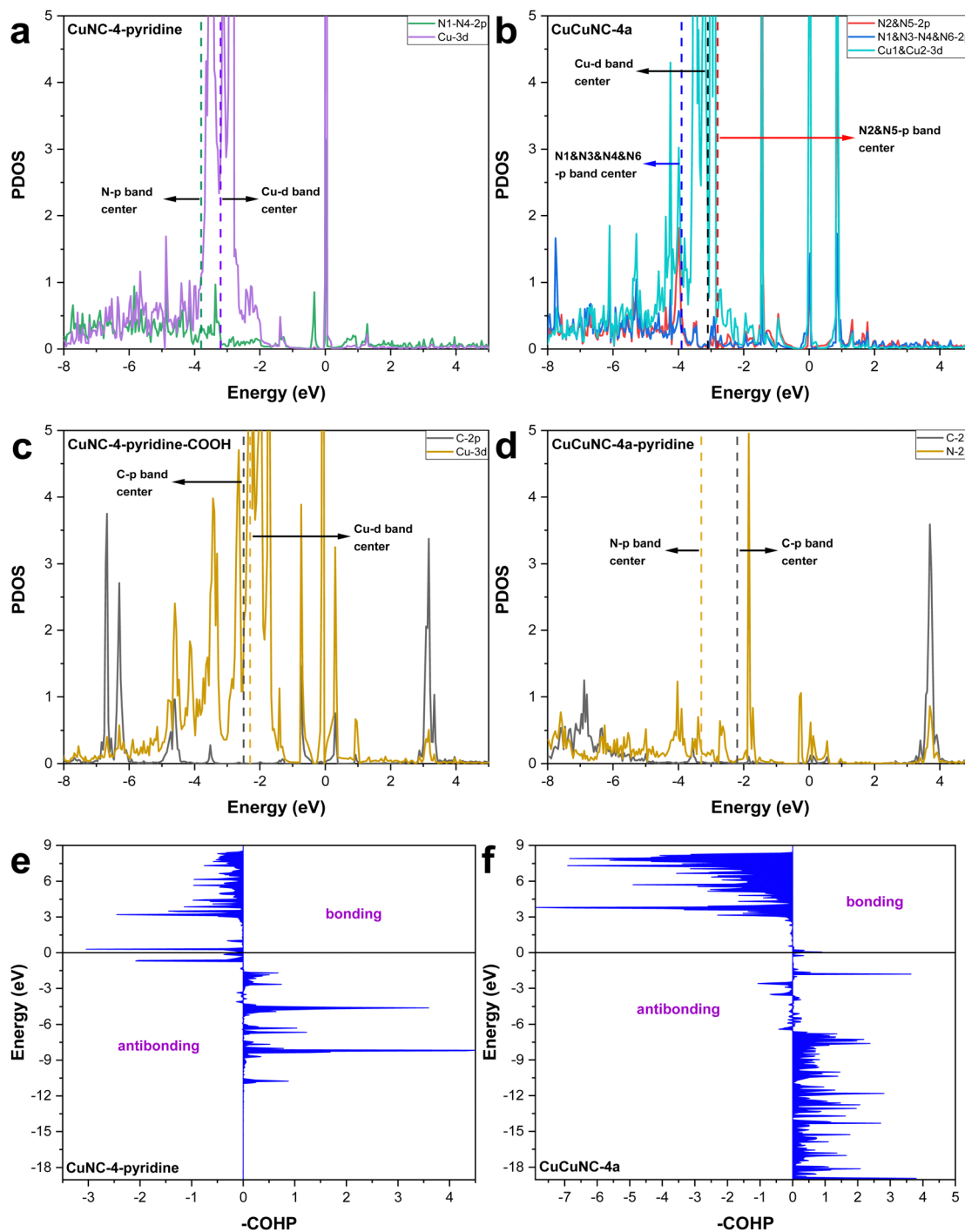


Fig. 7 Partial density of states (PDOS) of N and Cu atoms on (a) CuNC-4-pyridine and (b) CuCu-NC-4a. Partial density of states (PDOS) of adsorbed COOH on (c) CuNC-4-pyridine with Cu and C atoms and (d) CuCu-NC-4a with N and C atoms. Crystal orbital Hamilton population (COHP) between Cu–C on (e) CuNC-4-pyridine and (f) CuCu-NC-4a with the adsorption of *COOH.

of the products, resulting in more difficult detachment of the products, especially for C_2 chemicals. For product selectivity, based on the aforementioned analysis, CuCuNC-4a shows better performance in C_2 product formation than CuNC-4-pyridine. To sum up, CuCuNC-4a catalysts have high selectivity for C_2 products and a low limiting potential (high power utilisation), but the competitive H_2 formation reactions are

aggressive and the products are difficult to desorb from the catalyst.

Regarding the improvement of catalyst performance, it can be achieved by changing the central atom as well as the coordination environment, and incorporating alternative axial ligands or double-centre metal active sites.⁸ H_2 formation can also be inhibited by adjusting the pH values of the electrolyte,



Table 1 Summary of U_L and E_{ads} of the main products during the CO_2 electroreduction process on CuNC-1-pyridine and CuCuNC-4a

U_L (eV)	CuNC-4-pyridine	CuCuNC-4a	E_{ads} (eV)	CuNC-4-pyridine	CuCuNC-4a
H ₂	-0.8	-0.1	CO ₂	0.32	0.18
CO	-1.07	-0.22	CO	0.3	0.29
HCOOH	-0.44	-0.1	HCOOH	0.2	0.03
CH ₃ OH	-0.68	-0.51	CH ₃ OH	0.13	-0.05
CH ₄	-0.68	-0.51	CH ₄	0.41	0.23
C ₂ H ₆ O	-1.07	-0.36	C ₂ H ₆ O	-0.1	-0.19
C ₂ H ₄	-1.07	-0.36	C ₂ H ₄	1.44	-0.45
C ₂ H ₆	-1.07	-0.36	C ₂ H ₆	-0.26	-0.47

the pressure and temperature of gas phase CO_2 , or adopting non-aqueous solution.^{42,43} MNC materials can be synthesized by the following methods: pyrolysis, liquid phase exfoliation, electrochemical deposition, thermal synthesis and wet chemistry.⁸ Nitrogen doping of graphene may have different structures in the manufacturing process. And careful selection of the appropriate method and parameters is required when manufacturing target catalysts.

5. Conclusions

In the present study, we systematically explored the behaviours of Cu-SACs and Cu-DACs during the CO_2 electroreduction process using DFT calculations. Five robust structures are determined after testing the thermal and kinetic stabilities of eleven possible configurations. The performance of C-C coupling reactions on the selected catalysts was investigated. Results show that CuNC-4-pyridine and CuCuNC-4a can benefit C₂ chemical generation with negative energy changes in the C-C coupling process. Subsequently, the detailed mechanisms of C₁ and C₂ chemical formation (CO, HCOOH, CH₃OH, CH₄, C₂H₆O, C₂H₄ and C₂H₆) during CO_2 electroreduction on CuNC-4-pyridine and CuCuNC-4a are studied. CuCuNC-4a presents a high selectivity for C₂ products and a low limiting potential (high power utilisation), but competitive H₂ formation reactions are vigorous and the products are hard to desorb from the catalyst. The current research provides important insights for a thorough understanding and for potential design of MNC catalysts.

Conflicts of interest

There are no conflicts to declare.

Acknowledgements

Support from the UK Engineering and Physical Sciences Research Council under the project "UK Consortium on Meso-scale Engineering Sciences (UKCOMES)" (Grant No. EP/R029598/1 and EP/X035875/1) is gratefully acknowledged. This work made use of computational support by CoSeC, the Computational Science Centre for Research Communities, through UKCOMES.

References

- P. M. Vitousek, H. A. Mooney, J. Lubchenco and J. M. Melillo, Human domination of Earth's ecosystems, *Science*, 1997, 277(5325), 494–499.
- W.-H. Wang, Y. Himeda, J. T. Muckerman, G. F. Manbeck and E. Fujita, CO_2 hydrogenation to formate and methanol as an alternative to photo-and electrochemical CO_2 reduction, *Chem. Rev.*, 2015, 115(23), 12936–12973.
- Y. Lu, Z. Zhang, H. Wang and Y. Wang, Toward efficient single-atom catalysts for renewable fuels and chemicals production from biomass and CO_2 , *Appl. Catal., B*, 2021, 292, 120162.
- L. Fan, C. Xia, F. Yang, J. Wang, H. Wang and Y. Lu, Strategies in catalysts and electrolyzer design for electrochemical CO_2 reduction toward C²⁺ products, *Sci. Adv.*, 2020, 6(8), eaay3111.
- Z.-Q. Liang, T.-T. Zhuang, A. Seifitokaldani, J. Li, C.-W. Huang and C.-S. Tan, *et al.*, Copper-on-nitride enhances the stable electrosynthesis of multi-carbon products from CO_2 , *Nat. Commun.*, 2018, 9(1), 3828.
- T.-T. Zhuang, Z.-Q. Liang, A. Seifitokaldani, Y. Li, P. De Luna and T. Burdyny, *et al.*, Steering post-C-C coupling selectivity enables high efficiency electroreduction of carbon dioxide to multi-carbon alcohols, *Nat. Catal.*, 2018, 1(6), 421–428.
- L. Wang, L. Wang, J. Zhang, X. Liu, H. Wang and W. Zhang, *et al.*, Selective hydrogenation of CO_2 to ethanol over cobalt catalysts, *Angew. Chem., Int. Ed.*, 2018, 57(21), 6104–6108.
- T. Tang, Z. Wang and J. Guan, Optimizing the electrocatalytic selectivity of carbon dioxide reduction reaction by regulating the electronic structure of single-atom M-N-C materials, *Adv. Funct. Mater.*, 2022, 32(19), 2111504.
- A. Guan, Z. Chen, Y. Quan, C. Peng, Z. Wang and T.-K. Sham, *et al.*, Boosting CO_2 electroreduction to CH_4 via tuning neighboring single-copper sites, *ACS Energy Lett.*, 2020, 5(4), 1044–1053.
- D. Karapinar, N. T. Huan, N. Ranjbar Sahraie, J. Li, D. Wakerley and N. Touati, *et al.*, Electroreduction of CO_2 on single-site copper-nitrogen-doped carbon material: selective formation of ethanol and reversible restructuring of the metal sites, *Angew. Chem., Int. Ed.*, 2019, 58(42), 15098–15103.
- Y. Ouyang, L. Shi, X. Bai, Q. Li and J. Wang, Breaking scaling relations for efficient CO_2 electrochemical reduction through dual-atom catalysts, *Chem. Sci.*, 2020, 11(7), 1807–1813.
- K. Zhao, X. Nie, H. Wang, S. Chen, X. Quan and H. Yu, *et al.*, Selective electroreduction of CO_2 to acetone by single copper atoms anchored on N-doped porous carbon, *Nat. Commun.*, 2020, 11(1), 2455.
- X. Wei, S. Wei, S. Cao, Y. Hu, S. Zhou and S. Liu, *et al.*, Cu acting as Fe activity promoter in dual-atom Cu/Fe-NC catalyst in CO_2RR to C₁ products, *Appl. Surf. Sci.*, 2021, 564, 150423.
- G. Kresse and J. Furthmüller, Efficiency of ab initio total energy calculations for metals and semiconductors using a plane-wave basis set, *Comput. Mater. Sci.*, 1996, 6(1), 15–50.



- 15 G. Kresse and J. Hafner, Ab initio molecular dynamics for liquid metals, *Phys. Rev. B: Condens. Matter Mater. Phys.*, 1993, **47**(1), 558.
- 16 B. Hammer, L. B. Hansen and J. K. Nørskov, Improved adsorption energetics within density-functional theory using revised Perdew-Burke-Ernzerhof functionals, *Phys. Rev. B: Condens. Matter Mater. Phys.*, 1999, **59**(11), 7413.
- 17 S. Grimme, J. Antony, S. Ehrlich and H. Krieg, A consistent and accurate ab initio parametrization of density functional dispersion correction (DFT-D) for the 94 elements H-Pu, *J. Chem. Phys.*, 2010, **132**(15), 154104.
- 18 S. Grimme, S. Ehrlich and L. Goerigk, Effect of the damping function in dispersion corrected density functional theory, *J. Comput. Chem.*, 2011, **32**(7), 1456–1465.
- 19 J. K. Nørskov, J. Rossmeisl, A. Logadottir, L. Lindqvist, J. R. Kitchin and T. Bligaard, *et al.*, Origin of the overpotential for oxygen reduction at a fuel-cell cathode, *J. Phys. Chem. B*, 2004, **108**(46), 17886–17892.
- 20 A. A. Peterson, F. Abild-Pedersen, F. Studt, J. Rossmeisl and J. K. Nørskov, How copper catalyzes the electroreduction of carbon dioxide into hydrocarbon fuels, *Energy Environ. Sci.*, 2010, **3**(9), 1311–1315.
- 21 K. Mathew, V. C. Kolluru, S. Mula, S. N. Steinmann and R. G. Hennig, Implicit self-consistent electrolyte model in plane-wave density-functional theory, *J. Chem. Phys.*, 2019, **151**(23), 234101.
- 22 K. Letchworth-Weaver and T. Arias, Joint density functional theory of the electrode-electrolyte interface: application to fixed electrode potentials, interfacial capacitances, and potentials of zero charge, *Phys. Rev. B: Condens. Matter Mater. Phys.*, 2012, **86**(7), 075140.
- 23 K. Mathew, R. Sundararaman, K. Letchworth-Weaver, T. Arias and R. G. Hennig, Implicit solvation model for density-functional study of nanocrystal surfaces and reaction pathways, *J. Chem. Phys.*, 2014, **140**(8), 084106.
- 24 A. J. Garza, A. T. Bell and M. Head-Gordon, Mechanism of CO₂ reduction at copper surfaces: pathways to C₂ products, *ACS Catal.*, 2018, **8**(2), 1490–1499.
- 25 V. Wang, N. Xu, J.-C. Liu, G. Tang and W.-T. Geng, VASPKIT: A user-friendly interface facilitating high-throughput computing and analysis using VASP code, *Comput. Phys. Commun.*, 2021, **267**, 108033.
- 26 W. Yi, G. Tang, X. Chen, B. Yang and X. Liu, qvasp: a flexible toolkit for VASP users in materials simulations, *Comput. Phys. Commun.*, 2020, **257**, 107535.
- 27 S. Maintz, V. L. Deringer, A. L. Tchougréeff and R. Dronskowski, LOBSTER: A tool to extract chemical bonding from plane-wave based DFT, *J. Comput. Chem.*, 2016, **37**, 1030–1035.
- 28 S. Zhu, K. Wan, H. Wang, L.-J. Guo and X. Shi, The role of supported dual-atom on graphitic carbon nitride for selective and efficient CO₂ electrochemical reduction, *Nanotechnology*, 2021, **32**(38), 385404.
- 29 C. Guo, T. Zhang, X. Deng, X. Liang, W. Guo and X. Lu, *et al.*, Electrochemical CO₂ reduction to C1 products on single nickel/cobalt/iron-doped graphitic carbon nitride: a DFT study, *ChemSusChem*, 2019, **12**(23), 5126–5132.
- 30 S. Back and Y. Jung, TiC- and TiN-supported single-atom catalysts for dramatic improvements in CO₂ electrochemical reduction to CH₄, *ACS Energy Lett.*, 2017, **2**(5), 969–975.
- 31 J. H. Montoya, C. Tsai, A. Vojvodic and J. K. Nørskov, The challenge of electrochemical ammonia synthesis: a new perspective on the role of nitrogen scaling relations, *ChemSusChem*, 2015, **8**(13), 2180–2186.
- 32 W. Zou, R. Lu, X. Liu, G. Xiao, X. Liao and Z. Wang, *et al.*, Theoretical insights into dual-atom catalysts for the oxygen reduction reaction: the crucial role of orbital polarization, *J. Mater. Chem. A*, 2022, **10**(16), 9150–9160.
- 33 R. Hu, Y. Li, Q. Zeng and J. Shang, Role of active sites in N-coordinated Fe-Co dual-metal doped graphene for oxygen reduction and evolution reactions: a theoretical insight, *Appl. Surf. Sci.*, 2020, **525**, 146588.
- 34 H. Xu, D. Cheng, D. Cao and X. C. Zeng, A universal principle for a rational design of single-atom electrocatalysts, *Nat. Catal.*, 2018, **1**(5), 339–348.
- 35 X.-L. Lu, X. Rong, C. Zhang and T.-B. Lu, Carbon-based single-atom catalysts for CO₂ electroreduction: progress and optimization strategies, *J. Mater. Chem. A*, 2020, **8**(21), 10695–10708.
- 36 S. Li, A. Guan, C. Yang, C. Peng, X. Lv and Y. Ji, *et al.*, Dual-atomic Cu sites for electrocatalytic CO reduction to C²⁺ products, *ACS Mater. Lett.*, 2021, **3**(12), 1729–1737.
- 37 K. Zhao, X. Nie, H. Wang, S. Chen, X. Quan and H. Yu, *et al.*, Selective electroreduction of CO₂ to acetone by single copper atoms anchored on N-doped porous carbon, *Nat. Commun.*, 2020, **11**(1), 1–10.
- 38 A. Savin, R. Nesper, S. Wengert and T. F. Fässler, ELF: The electron localization function, *Angew. Chem., Int. Ed. Engl.*, 1997, **36**(17), 1808–1832.
- 39 J. H. Liu, L. M. Yang and E. Ganz, Two-Dimensional Organometallic TM₃-C₁₂S₁₂ Monolayers for Electrocatalytic Reduction of CO₂, *Energy Environ. Mater.*, 2019, **2**(3), 193–200.
- 40 S. Wang, W. Ma, Z. Sang, F. Hou, W. Si and J. Guo, *et al.*, Dual-modification of manganese oxide by heterostructure and cation pre-intercalation for high-rate and stable zinc-ion storage, *J. Energy Chem.*, 2022, **67**, 82–91.
- 41 S. Liu, B. Zhang, L. Zhang and J. Sun, Rational design strategies of Cu-based electrocatalysts for CO₂ electroreduction to C₂ products, *J. Energy Chem.*, 2022, **71**, 63–82.
- 42 H. Shen, Y. Li and Q. Sun, CO₂ electroreduction performance of phthalocyanine sheet with Mn dimer: a theoretical study, *J. Phys. Chem. C*, 2017, **121**(7), 3963–3969.
- 43 Y. Hori, Electrochemical CO₂ reduction on metal electrodes, *Mod. Aspects Electrochem.*, 2008, 89–189.

